ACS Catalysis
Research Article
pubs.acs.org/acscatalysis

Supportless, Bismuth-Modified Palladium Nanotubes with Improved Activity and Stability for Formic Acid Oxidation

Robert W. Atkinson, III,[†] Samuel St. John,[†] Ondrej Dyck,[†] Kinga A. Unocic,[⊥] Raymond R. Unocic,[‡] Colten S. Burke,[§] Joshua W. Cisco,[§] Cynthia A. Rice,[§,∥] Thomas A. Zawodzinski, Jr.,[†,⊥] and Alexander B. Papandrew*,[†]

[†]Department of Chemical and Biomolecular Engineering, University of Tennessee, Knoxville, Tennessee 37996, United States
[‡]Center for Nanophase Materials Sciences, Oak Ridge National Laboratory, Oak Ridge, Tennessee 37831, United States
[§]Department of Chemical Engineering, Tennessee Technological University, Cookeville, Tennessee 38505, United States
[∥]Center for Manufacturing Research, Tennessee Technological University, Cookeville, Tennessee 38505, United States
[⊥]Materials Science and Technology Division, Oak Ridge National Laboratory, Oak Ridge, Tennessee 37831, United States

Ⓢ *Supporting Information*

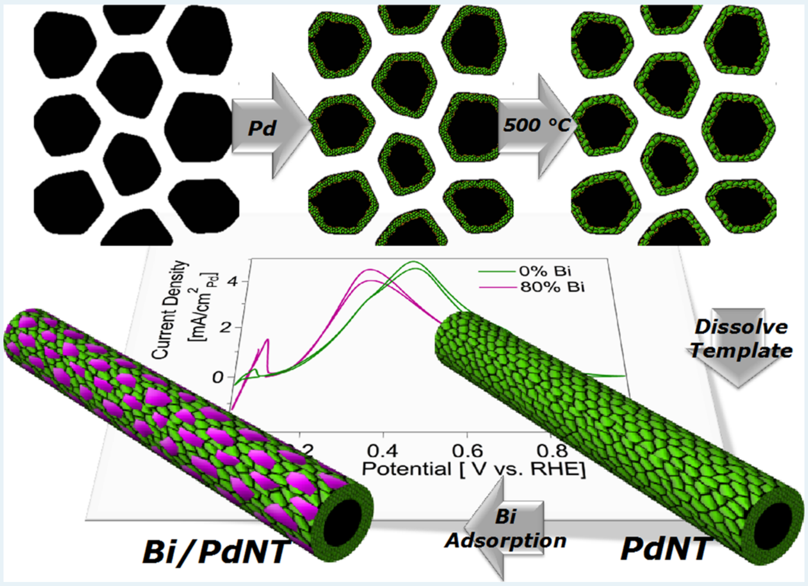

ABSTRACT: Palladium nanotubes (PdNTs) were synthesized by templated vapor deposition and investigated for formic acid electrooxidation. Annealed PdNTs are 2.4 times more active (2.19 mA/cm^2) than commercial carbon-supported palladium (0.91 mA/cm^2) at 0.3 V vs RHE. Bismuth modification improved nanotube performance over 4 times (3.75 mA/cm^2) vs Pd/C and nearly 2 times vs unmodified PdNTs. A surface Bi coverage of 80% results in optimal site-specific activity by drastically reducing surface-poisoning CO generation during formic acid electrooxidation. The Bi-modified PdNTs are exceptionally stable, maintaining 2 times the area-normalized current density as Pd/C after 24 h at 0.2 V vs RHE. We attribute the enhanced activity and stability of the nanotube catalysts to the presence of highly coordinated surfaces, mimicking a flat polycrystal while retaining high surface area geometry.

KEYWORDS: *formic acid oxidation, palladium nanotube, bismuth adatom, chemical vapor deposition, templated synthesis, anodic alumina*

1. INTRODUCTION

The growing market for portable and mobile devices has driven the demand for small, light, long-lasting power sources. Direct liquid fuel cells (DLFCs) have the potential to compete with current battery technology in these arenas because of the high volumetric energy density of liquid fuels. Formic acid is an attractive fuel option that is nontoxic, nonflammable, and can be used in highly concentrated fuel feed streams without the crossover observed in direct methanol fuel cells (DMFCs).[1,2]

A common shortcoming of DLFCs is low efficiency due to the high overpotential typically required for fuel oxidation. Here, we

Received: June 12, 2015
Revised: July 22, 2015
Published: July 22, 2015

DOI: 10.1021/acscatal.5b01239
ACS Catal. 2015, 5, 5154−5163

use overpotential to refer to the additional applied voltage beyond the thermodynamic requirement needed for an electrochemical reaction to proceed, that is, for current to flow. In many cases, an applied overpotential affects the removal of adsorbed species from the catalyst surface. This is the case in both DMFCs and direct formic acid fuel cells (DFAFCs), for which anode catalyst poisoning by CO is a deactivation channel (eq 1).[3] However, a direct reaction pathway (eq 2)[3] is accessible, depending on the adsorption orientation of formic acid.[4] Designing catalysts selective for this path is thus the key to enabling efficient DFAFCs.

Indirect pathway (overpotential > 0.6 V):[4]

$$\mathrm{HCOOH} \rightarrow \mathrm{CO}_{\mathrm{ads}} + \mathrm{H_2O} \rightarrow \mathrm{CO_2} + 2\mathrm{H}^+ + 2\mathrm{e}^- \tag{1}$$

Direct pathway (overpotential >0.18 V):[5]

$$\mathrm{HCOOH} \rightarrow \mathrm{CO_2} + 2\mathrm{H}^+ + 2\mathrm{e}^- \tag{2}$$

Palladium has been shown to be highly active for formic acid electro-oxidation at low overpotentials because it favors the direct pathway;[6] however, Pd lacks sustained performance from the accumulation of CO_{ads} that can form from competition by the indirect pathway.[7−11] Modifying Pd to promote its activity at low overpotentials and to improve its stability by limiting CO_{ads} formation is essential. Strategies centered on alloying to remove CO_{ads} generated by the indirect pathway have been described previously.[6,12−18]

The addition of adatoms to the catalyst surface, such as Bi or Sb, has been shown to improve formic acid electro-oxidation activity at low overpotentials by so-called ensemble or third-body effects.[4,5,19−25] Coupled in situ surface-enhanced infrared spectroscopy and first-principles density functional theory calculations indicate that the addition of adatoms can influence the configuration of the formic acid molecule at the catalyst surface.[4] High adatom coverage can promote the adsorption of formic acid in the CH-down configuration[4] that is considered the precursor for the direct formic acid oxidation (FAO) pathway and high activity at low overpotentials.[26−30]

The less desirable indirect pathway for formic acid oxidation requires a larger ensemble of metal atoms than the direct pathway;[25,26] therefore, a high adatom coverage that effectively reduces the Pd ensemble size can improve formic acid electro-oxidation activity at low overpotentials. Because active catalyst surface area is lost to the adsorbed adatom, having a high proportion of adjacent low-index sites is paramount when pursuing strategies that use adsorbed promoter atoms. High-surface-area catalysts do not provide sufficient surface area for Bi adsorption adjacent to active sites for formic acid adsorption because they have small terraces. In addition, these catalysts lose half of their surface to low-coordination edge and vertex sites.[31]

An alternative to supported nanoparticle catalysts is unsupported extended-surface catalysts, such as metallic nanowires or nanotubes. Metallic nanotubes have many similarities to bulk polycrystalline materials while maintaining nanoscale dimensionality, allowing very high activities while limiting sacrifices in the active surface area. Extended surface catalysts have highly coordinated surfaces that are more resistant to corrosion and ripening,[31−36] reduced oxophilicity, and binding of oxygenated intermediates[37−39] and significant flexibility to achieve optimal porous structure via heat treatment.[40−42] In this contribution, we describe palladium nanotubes (PdNTs) designed to mimic highly coordinated polycrystalline surfaces but with nanoscale dimensions and mesoporosity. As a result, the nanotubes maintain a high surface area without the formation of an undercoordinated surface associated with reductions in nanoparticle size.[43] This was achieved via the use of a modified chemical vapor deposition technique to synthesize the PdNTs within sacrificial, porous alumina templates. The morphology and grain size of the nanotubes were adjusted by thermal treatments of the Pd-lined templates using postdeposition heat treatment. The sacrificial templates were dissolved to release unsupported nanotubes. Electrochemical bismuth adsorption was subsequently used to systematically probe the coverage-dependent steric effects for the promotion of the direct electrooxidation of formic acid.

2. EXPERIMENTAL SECTION

Nanotube Synthesis. PdNTs were synthesized by a chemical vapor deposition within the pores of an anodic alumina membrane (Whatman Anodisc, 13 mm diameter, 200 nm pore size) by a technique reported previously.[40] A powder of palladium(II)(2,4)-pentanedionate (Alfa Aesar), so-called palladium acetylacetonate, was confined beneath the alumina template and placed in a vacuum oven with 2.3 mL of deionized water. Air was evacuated from the oven by a rotary vane vacuum pump and replaced with dry N_2 several times before the pressure was reduced to 0.3 bar and the oven was sealed. The thermostat was set to a calibrated value of 170 °C, and this final temperature was maintained for 15 h before the oven was flushed with dry N_2 and cooled to room temperature to recover the Pd-filled template.

The Pd-bearing templates were either immediately dissolved to recover as-synthesized PdNTs or thermally annealed to induce morphological evolution. After purging a quartz furnace tube for 30 min, the sample templates were heated at one of a range of temperatures for 1 h with flowing 4% H_2 (balance Ar) before they were allowed to cool passively to room temperature. The temperatures selected for the heat treatments were 300, 400, and 500 °C.

The sample templates were stirred in a 30% KOH solution at room temperature for 90 h to completely dissolve the templates. Afterward, the supernatant solution was decanted and replaced with deionized water until the nanotubes were suspended in a solution with neutral pH.

Scanning Electron Microscopy. SEM micrographs were collected using a Zeiss 1525 field emission scanning electron microscope with an accelerating voltage of 3 kV using the in-lens electron detector.

Transmission Electron Microscopy. Thin cross sections of the nanotubes within the alumina template were prepared using a Hitachi NB-5000 focused ion beam. High-angle annular dark-field (HAADF) scanning transmission electron microscopy (STEM) imaging and EDS mapping were conducted using a JEOL 2200FS operating at 200 kV. Nanotubes liberated from the sacrificial template and suspended in water were drop-cast onto lacy carbon and dried under vacuum to collect high-resolution transmission electron microscopy (HRTEM) images with a Zeiss Libra 200MC at an accelerating voltage of 200 kV.

X-ray Diffraction. X-ray diffraction (XRD) patterns were recorded with a Bruker D2 Phaser diffractometer with Cu Kα radiation ($\lambda = 0.1541874$ nm, 30 kV, 10 mA, 0.014° step, 0.5 s/step). Small aliquots of the nanotubes suspended in water were cast onto a zero-background silicon wafer for data collection. The diffraction peaks were fit using a Voigt function with IGOR Pro (Wavemetrics, Inc.) allowing for determination of their positions and widths.

X-ray Absorption Spectroscopy. X-ray absorption spectroscopy was conducted at beamline 20-BM at the Advanced Photon Source at Argonne National Laboratory (Argonne, IL, USA). Pre-edge correction, normalization, and postedge subtraction via spline fitting were done in Athena.[44] The k^2-weighted $\chi(R)$ forward Fourier transform (FT) parameters were R range, 1−3 Å; window, Hanning.

Electrochemical Measurements. Electrode inks were prepared by diluting the water-suspended nanotubes to 0.65−0.80 mg_{Pd} mL^{-1} without the addition of alcohol or ionomer, as is common for carbon-supported, high-surface-area catalysts.[45] Measurements were conducted with a glassy carbon working electrode, platinum wire counter electrode and a reversible hydrogen reference electrode (RHE) using a Bio-Logic VMP3 potentiostat. All electrolytes were purged with ultrahigh purity N_2 for 30 min prior to experiments.

Carbon monoxide stripping voltammograms were recorded in 0.5 M H_2SO_4 via a technique described elsewhere[5,46] to calculate electrochemically active surface areas (ECSAs). The ECSAs were calculated using the charge for removing a monolayer of CO from a Pt surface (420 μC cm^{-2}).[47] FAO activity was measured by cycling the electrode once in fresh 0.5 M formic acid (HCOOH, Fluka Analytical, for HPLC) and 0.5 M H_2SO_4 at 20 mV s^{-1}. Chronoamperometry experiments were performed in 1.0 M formic acid and 0.1 M $HClO_4$ (GFS Chemicals, Veritas) with the potential held at 0.2 V vs RHE for 24 h without rotation. Cyclic voltammograms were recorded before and after chronoamperometry experiments to study changes in the catalysts after long-term stability experiments. Although such experiments were not conducted in this work, the analysis of the electrolytes used in the chronoamperometry experiments via inductively coupled plasma mass spectrometry (ICP−MS) would allow for accurately quantifying the amounts of Pd and Bi that dissolve from the electrode. This will be considered as a subject of future study.

Carbon-supported Pd (Pd/C, Alfa Aesar, 20 wt % Pd) was used as a standard for comparison of the performance of the experimental catalysts. The commercial catalyst (5 mg) was dispersed in 3:1 water/isopropyl alcohol solvent mixture (4 mL) containing 5 mg of Nafion from a 5% solution (Ion Power, Inc.).

Bismuth adatoms were underpotentially deposited on PdNTs annealed at 500 °C. An electrode with PdNTs was immersed in a 0.5 mM $Bi_2(SO_4)_3$ (Alfa Aesar, 99%) and 0.5 M H_2SO_4 electrolyte with a constant potential (0.485−0.735 V vs RHE) held for 2 min, depending on the desired adatom coverage. This method is notable for its difference in comparison with spontaneous deposition of Bi onto Pt surfaces without the need for applying a potential. Such spontaneous deposition onto Pt is well-known and has been used to quantify Pt(111) contributions to surface area on polycrystalline surfaces.[48−51] The Bi surface coverage was determined using CO stripping voltammetry with a method reported previously.[20] The ECSA used to normalize currents for the Bi-modified PdNTs refers to the Pd without adsorbed Bi available for carbon monoxide adsorption.

3. RESULTS AND DISCUSSION

Conformal coatings of Pd are vapor-grown within the channels of a porous anodic alumina template to form the high aspect ratio, metallic Pd nanotubes. HAADF STEM and EDS map images for cross sections of the Pd nanotubes still embedded within the alumina template are shown in Figure 1. The aluminum (b, f) and oxygen (c, g) maps in Figure 1 identify the porous alumina template, which supports a thin layer of vapor-deposited Pd (d, h). In the as-synthesized sample template in Figure 1(a−d), the fine Pd nanoparticles form a conformal layer along the interior pores of the anodic alumina template. After heat treatment at 500 °C for 1 h, the thickness of the Pd deposit decreases while still conforming to the template pore walls, reflecting reductions in nanotube wall thickness that accompany the transition from loosely associated nanoparticle aggregates toward Pd grain growth to form a polycrystal-like surface. The nanotube samples were harvested for further study of their microstructures and for electrochemical characterization by dissolving the sacrificial template in KOH.

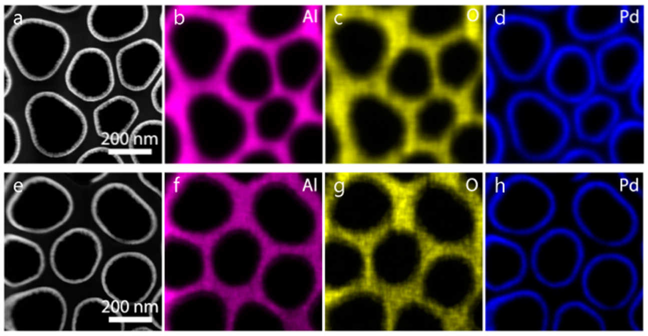

Figure 1. HAADF STEM and EDS elemental mapping of the templated (a−d) as-synthesized PdNTs and (e−h) PdNTs annealed at 500 °C.

The HRTEM images in Figure 2 show subtle changes in the microstructures of the PdNTs that are a result of thermal annealing. The as-synthesized PdNTs (Figure 2a,b) are best described as loosely aggregated and fine Pd nanoparticles. As a result, these nanotubes were less robust than the annealed PdNTs, manifested by a greater frequency of shortened and broken nanotubes. The morphologies of the PdNTs annealed at 300 °C (Figure 2c,d) and 400 °C (Figure 2e,f) are nearly indistinguishable aside from a marginal increase in Pd grain size. These annealed nanotubes more consistently maintain high-aspect ratio, tubular microstructures compared with the as-synthesized nanotubes, which may be the result of incremental Pd particle growth that occurred during heat treatment. The changes between the PdNTs annealed at 400 and 500 °C are more distinct, however. The PdNTs annealed at 500 °C (Figure 2g,h) are the most coarse-grained and have the highest degree of nanoporosity. The fast Fourier transform (FFT) of the boxed region in Figure 2h is represented in the image inset and is consistent with face-centered cubic (FCC) palladium.

The nanotube morphology is consistent with the shapes of the pore interiors of the AAO templates in which they were grown, as illustrated using the SEM images in Figure 3. The nanotubes reported here, although having a different composition, have a nanoscale structure remarkably similar to previously investigated samples.[40,42] The PdNTs are roughly 250 nm in diameter with variable lengths ranging from 1 to 10 μm. There is a growth in grain size, observable upon careful inspection here and more clearly in the HRTEM images in Figure 2, from the as-synthesized PdNT (Figure 3a) to the annealed PdNTs. In the SEM images in Figure 3, this grain growth is manifested by changes in texture of the nanotube surfaces. At these magnifications, the nanoparticles are unresolvable in the as-synthesized PdNTs and give the surfaces of these relatively thick-walled nanotubes a fine, nanoparticulate texture. After heat treatments at 300 °C (Figure 3b) and 400 °C (Figure 3c) individual grains can be resolved, fine nanoscale porosity is initiated, and the exterior surfaces become

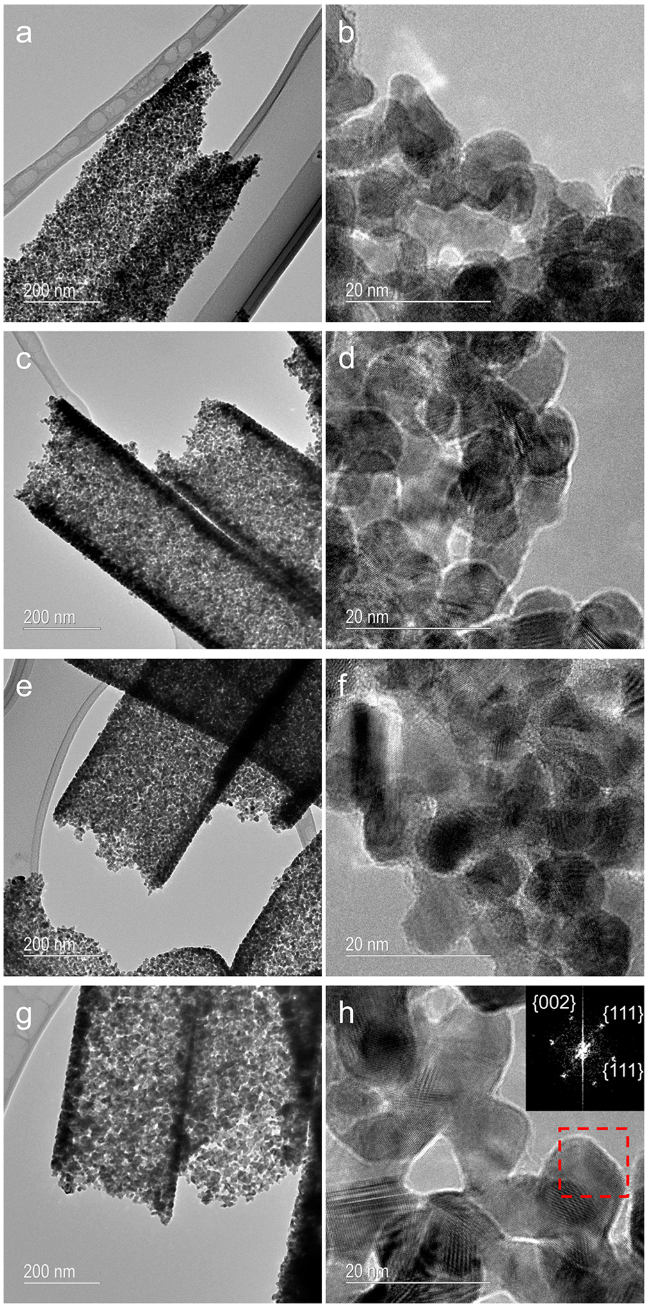

Figure 2. High-resolution transmission electron microscopy images of PdNTs (a,b) as-synthesized and after heat treatments in 4% H_2 for 1 h at (c,d) 300 °C, (e,f) 400 °C, and (g,h) 500 °C. FFT analysis from the boxed region in panel h corresponds to crystalline, FCC Pd oriented along the [110] zone axis.

more smooth. After annealing at 500 °C (Figure 3d), we observe a maximum in porosity, a reduction in nanotube wall thickness from 30 to roughly 20 nm, and a maximum in grain size for the nanotube samples.

The PdNT X-ray diffraction patterns were studied to measure the initial Pd grain sizes formed during synthesis as well as to study the influence of temperature on grain growth during the heat treatment. Cu Kα X-ray diffraction patterns are given in Figure 4. The as-synthesized PdNTs are characterized by broad FCC peaks, indicating that the nanotubes are aggregates of finely packed, nanoparticulate Pd, with an average grain size of 3.7 nm in diameter. The diffraction patterns of the annealed samples increase in sharpness (i.e., reduction of the peak's full-width at half its maximum, fwhm) with increasing heat treatment temperature, reflecting increases in grain size that are observable in the HRTEM and SEM images in Figures 2 and 3, respectively. We calculate a maximum Pd grain size of 11.6 nm after annealing at 500 °C. The average grain sizes for each sample are calculated using a Scherrer analysis of the Pd(111) peak and are reported in Table 1.

The primary diffraction peak of the as-synthesized PdNT is shifted relative to the reference Pd(111) peak because of absorption of interstitial carbon from the decomposition of the

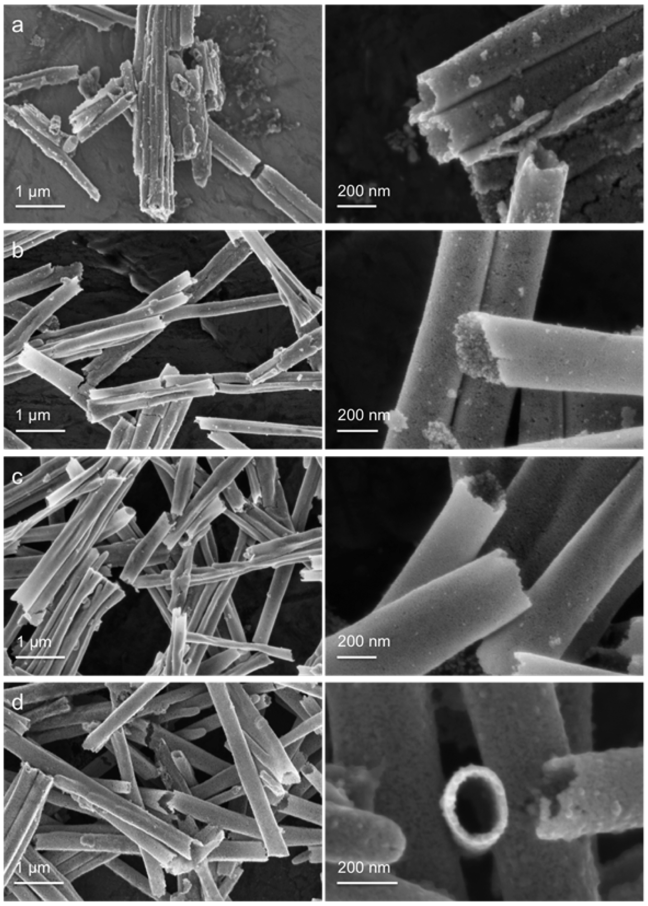

Figure 3. SEM images of PdNTs (a) as-synthesized and after heat treatments in 4% H_2 for 1 h at (b) 300, (c) 400, and (d) 500 °C. Increases in grain size are observed with increasing heat treatment temperature. Grain size estimates are provided in the text using XRD data.

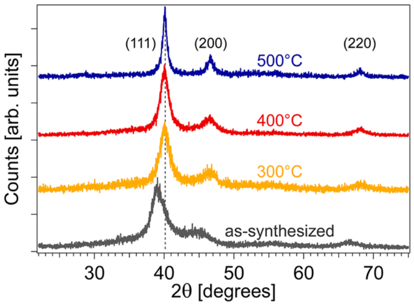

Figure 4. Cu Kα X-ray diffraction patterns for as-synthesized PdNTs and after annealing in 4% H_2 at 300, 400, and 500 °C for 1 h. Dashed line corresponds to Pd(111) peak (PDF: 00-005-0681).

Table 1. Location of Pd(111) Peak, Grain Size (*L*) Measured by Scherrer Analysis of the Pd(111) Peak, Electrode Loading, Electrochemical Surface Area (ECSA), and FAO Mass and Specific Activities at 0.3 V vs RHE

sample	heat treatment, °C	Pd[111] 2θ (deg)	L (nm)	loading ($\mu g_{Pd}/cm^2$)	ECSA (m^2/g)	i_s (0.3 V) (mA/cm^2)	i_m (0.3 V) (A/g_{Pd})
300 °C PdNT	300	40.060	4.9	38.63	29.6	1.56	461.8
400 °C PdNT	400	40.042	5.8	36.91	30.7	1.83	561.8
500 °C PdNT	500	40.084	11.6	38.21	24.7	2.19	540.9
Bi ~ PdNT (80%)	500	40.084	11.6	39.07	10.0	3.75	375.0
Pd/C		40.201	3.5	38.21	65.4	0.91	595.1

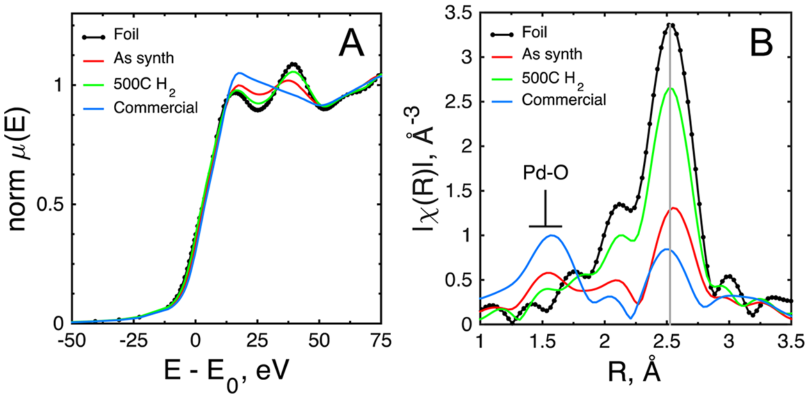

Figure 5. (A) Normalized XANES patterns for the as-synthesized and heat-treated PdNT samples, as well as commercial Pd/C compared with foil at the Pd K edge. (B) Forward Fourier transforms of the EXAFS at the Pd K edge. Gray line indicates Pd−Pd radial position. The lattice expansion due to carbon absorption in the as-synthesized sample is reflected in EXAFS as a shift to larger Pd−Pd radial position. The shift in the Pd peak of the commercial Pd/C to lower radial position reflects its high degree of oxidation and the smaller atomic size of Pd^{2+} (here observed as PdO).[57]

organic ligand during vapor deposition.[52−54] Carbon increases the size of the Pd lattice by inserting into interstitial sites, observed here as a decrease in the inversely related diffraction angle. The lattice expansion from interstitial carbon has been observed previously in other Pd catalysts that were synthesized by our group using this technique.[55,56] The return of the primary peak to the location of the Pd(111) peak in the reference reflects the removal of interstitial carbon during heat treatment.

Results from X-ray absorption spectroscopy are used to reveal the changes in atomic-scale structure and evolution during heat treatment and to compare with the commercial Pd/C catalyst. The X-ray absorption near-edge structure (XANES) patterns in Figure 5A illustrate that both nanotube samples have electronic character similar to the zerovalent Pd foil, whereas the increased white-line intensity of Pd/C and shift to higher energy suggests that it is highly oxidized. The forward Fourier transforms of the extended X-ray absorption fine structure (EXAFS) oscillations in Figure 5B yield the radial positions of the nearest neighbors of the Pd absorber. The Pd−Pd radial position in the as-synthesized nanotubes show increased atomic spacing consistent with interstitially absorbed carbon.[53] Following heat treatment, the Pd−Pd radial position shifts back to match that of the Pd reference foil (gray line, Figure 5B). As the Pd grain size/atomic coordination increases, the magnitude of the Pd−O interaction decreases. This is indicated in Figure 5B by a reduction in peak intensity at a radial position of ~1.5 Å. This reproduces the well-known effect that more highly coordinated surfaces are less oxophilic that is also observed in cyclic voltammograms in sulfuric acid.

Because of reductions in nanotube oxophilicity, we expect that electrochemical surface oxides and poisons (e.g., CO) would be more easily removed from the PdNTs when compared with commercial Pd/C catalysts. Evidence of this weaker adsorption of oxygen-containing species by the catalyst surface can be observed in the positive shift of the palladium oxide reduction peak (Figure 6A inset) in the reverse scan.[58] The 500 °C annealed PdNTs feature a more positively shifted palladium oxide reduction feature than the nanotubes annealed at 300 and 400 °C from a grain size increase at elevated temperatures; this behavior is also observed in platinum catalysts with increasing Pt crystallite size.[58−60]

The reduced oxophilicity of the nanotube catalysts also affects CO removal. There is a significant decrease in the potentials of the CO stripping peaks for the palladium nanotube samples in comparison with the Pd/C (see Figure 6B). This has been attributed to greater surface mobility of oxygen-containing species that are less strongly bound to extended surface catalysts in comparison with small, supported nanoparticles.[37,39,46]

The 500 °C PdNT sample features a small CO oxidation feature at lower potential than the main CO stripping peak. This preignition feature has been observed in extended Pt catalysts[37,39] and is reported to result from defect sites located at grain boundaries.[61] The presence of a grain-boundary-like component emphasizes that the annealed nanotube catalysts are close analogs to polycrystalline surfaces. This highlights a considerable advantage to the application of these metallic nanotubes because highly active surfaces may be synthesized with nanoscopic dimensions that limit sacrifices in surface area.

Although hydrogen absorption and adsorption processes occur in the same potential region, the anodic peak at 0.1 V is reported to be dominated by the desorption of absorbed hydrogen.[62] The increase in current density of the anodic peak at 0.1 V with heat treatment temperature in the PdNT samples may correspond to an increase in hydrogen absorption by the nanotubes with coarsened Pd grains because hydrogen absorption is more stable and abundant in larger Pd grains.[62,63] Palladium electrodes report inaccurate hydrogen underpotential deposition (H_{UPD}) charges because of this subsurface hydride

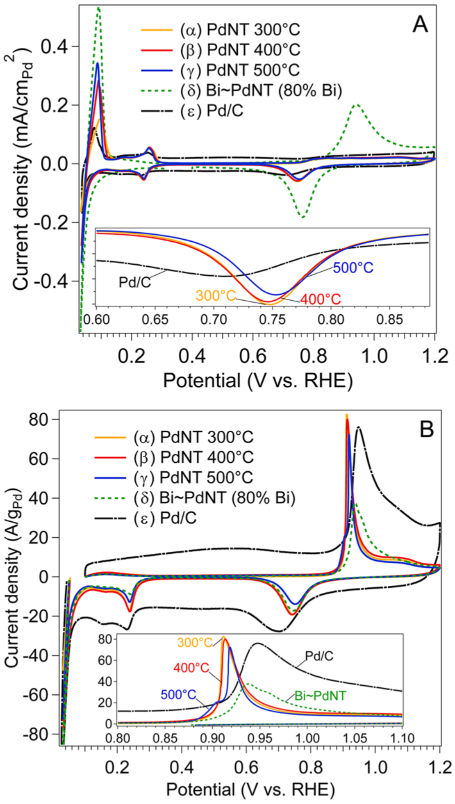

Figure 6. (A) Baseline cyclic voltammograms and (B) CO stripping voltammograms recorded in 0.5 M H_2SO_4 for the PdNTs annealed at (α) 300, (β) 400, (γ) 500 and (δ) 500 °C with 80% Bi surface coverage (Bi ~ PdNT), and (ε) carbon-supported Pd. The inset in (A) highlights the Pd oxide reduction region. The inset in (B) magnifies the CO stripping peaks.

formation, which produces current additional to H_{UPD} surface charging currents in the same potential region.[64,65] Therefore, the ECSA was determined by normalizing the charge of the CO stripping peak by the charge corresponding to the removal of a monolayer of preadsorbed CO from the catalyst surface, 420 μC cm^{-2}; these ECSAs are reported in Table 1.

Compared with the Bi-free PdNTs, the Bi-modified PdNTs (Bi ~ PdNT) with 80% Bi coverage (Figure 6,δ) have nearly eliminated charging from H_{UPD} because of interference from adsorbed Bi adatoms. In addition, there is a reversible Bi oxidation/reduction feature at 0.94−0.77 V vs RHE. The degree of Bi surface coverage of Pd is determined using the charges from the Bi oxidation peak and its CO stripping peak with a method adapted by Bauskar and Rice[20] from techniques used for Bi-modified Pt electrodes.[66]

The PdNTs annealed at 500 °C that have been modified with surface Bi adatoms (Figure 6B,δ) have a unique CO stripping feature that demonstrates CO stripping from free Pd surface sites in addition to Bi oxidation, occurring in the same potential range. The CO stripping voltammogram for the Bi-modified sample peaks at 0.94 V, with a broad shoulder at higher potentials (0.97 V) from the oxidation of Bi, which is also visible in the baseline voltammogram in Figure 6A(δ).

The addition of Bi adatoms to the catalyst surface reduces the Pd ensemble size, which is considered to promote FAO activity at low potentials[25,26] compared with a surface free of adatoms. In Figure 7, the formic acid oxidation voltammogram of unmodified PdNTs (Figure 7a) is compared with voltammograms of PdNTs after the adsorption of Bi adatoms to 42% and 80% coverage. At an intermediate coverage of 42% Bi (Figure 7b), we observe a reduction in specific activity compared with the unmodified PdNTs at 0.3 V, despite a cathodic shift of the potential for their peak FAO current. Increasing the Bi coverage to 80% results in both increased specific activity at low potential and a more negative shift in peak current potential for FAO. Together, these observations suggest that at high Bi coverages, a highly active ensemble of Pd active sites has formed on the catalyst surface that enhances FAO activity.

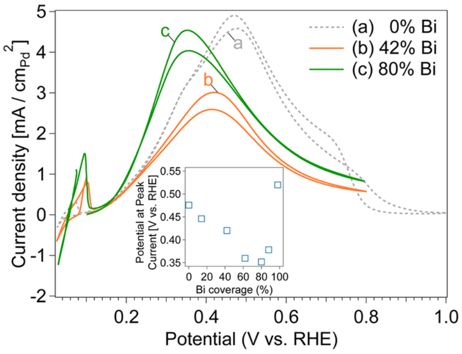

Figure 7. Area-normalized cyclic voltammograms recorded at 20 mV/s in 0.5 M H_2SO_4 and 0.5 M HCOOH for (a) PdNTs annealed at 500 °C prior to Bi coverage and with (b) 42% Bi and (c) 80% Bi coverage. Voltammograms are normalized to the available Pd area. Labels point to forward scans of voltammograms. The inset plots the potential of the peak current in the anodic scan as a function of Bi coverage.

This activity improvement at high adatom coverages is consistent with computational and experimental data for an ensemble, or third-body, effect.[19] The inset in Figure 7 reports the potential for the peak FAO current density in the anodic scan as a function of Bi coverage. As the Bi adatom coverage increases, the potential of the peak FAO current density decreases until the optimal adatom coverage of 80% Bi is reached. At higher Bi coverages (>88% Bi), the FAO peak current shifts back to higher potentials. The addition of Bi adatoms to these PdNTs improves their FAO activity significantly at low overpotentials, which suggests their promise for improvements in long-term FAO stability.

We studied the effect of Bi adatom coverage of the PdNT surface on formic acid oxidation activity and found an optimum surface coverage of Bi at 80%. The scatter plot in Figure 8 reports the specific activity at 0.3 V vs RHE as a function of Bi coverage on the PdNTs. There is an observed decrease in specific activity with a low Bi coverage (<40%) because the Bi adatoms cover and deactivate surface Pd sites. This reduction in activity suggests that there is not a significant electronic effect from the Bi on the PdNTs at this low surface coverage; otherwise, a small amount of surface Bi coverage would still be expected to enhance the FAO activity.[19] At this low Bi coverage, there may not be a sufficient amount of Bi on the surface to promote a considerable third-body effect.

At high Bi coverage (50−87.5%), the specific activity is increased compared with the activity measured for the unmodified PdNTs (orange dashed line, 2.18 mA/cm^2), peaking in FAO activity at 80% Bi coverage (3.75 mA/cm^2). The specific activity improvement indicates that the intrinsic activity of the catalyst at low potential is increased only when a high Bi coverage is obtained, consistent with a third-body effect.[19] High Bi coverages here may restrict the Pd ensemble size to fewer atoms than is suggested to be required for the undesirable pathway of FAO that is not active at low overpotentials.[25,26,67]

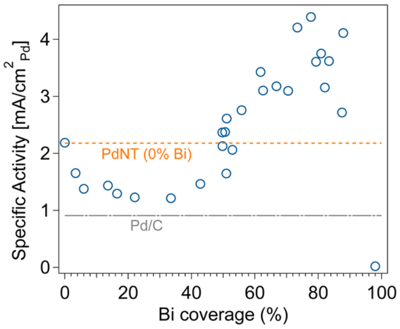

Figure 8. Scatter plot of specific activity of PdNTs as a function of their surface Bi coverage (in percent). The specific activity is reported at 0.3 V vs RHE from voltammograms recorded in 0.5 M H_2SO_4 and 0.5 M HCOOH at 20 mV/s. The orange dashed line corresponds to the specific activity of unmodified, 500 °C PdNTs, and the gray dashed–dotted line represents the specific activity of Pd/C, both also reported at 0.3 V vs RHE. Specific activity is normalized to the available Pd area.

It is important to note that the specific activity reported here is calculated using an ECSA that is defined by the remaining exposed surface Pd sites, which are those not already covered by Bi. At very high Bi adatom coverages (>87%), the remaining active sites are likely less accessible as the surface becomes more saturated with Bi,[5] thus interfering with formic acid adsorption and oxidation on these Pd surfaces.

We observe similar trends in the mass activity of PdNTs, shown in Figure S1 in the Supporting Information, as a function of Bi coverage. Owing to the high activity of Pd for the oxidation of formic acid, any amount of Bi added to the surface of the PdNTs in an attempt to improve the stability and resistance to poison formation of the catalyst results in a sacrifice of Pd active sites and a reduction in mass activity. For the Bi-modified PdNTs with Bi coverage of 62–74%, we observe a maximum mass activity of 397 A/g_{Pd}. Although this is a significant decrease in the mass activity compared with the Bi-free PdNTs (541 A/g_{Pd}), the influence of a third body effect from the addition of Bi adatoms to high coverage on the PdNTs promises improvements in stability by limiting the formation of poisoning intermediates.[25,26]

Prior to the addition of Bi adatoms, the annealed PdNTs are highly active for formic acid oxidation and have considerably higher specific activities than the commercial, carbon-supported Pd catalyst. Cyclic voltammograms of area-normalized currents for the electro-oxidation of formic acid by annealed and Bi-modified PdNTs are compared with Pd/C in Figure 9. The PdNTs annealed at 500 °C have nearly 2.5 times the specific activity and a mass activity comparable to that of the commercial Pd/C, despite reductions in the electrochemically active surface area. The specific and mass activities of the experimental and commercial catalysts are reported in Table 1.

The formic acid oxidation activity of the PdNTs increased with increasing heat treatment temperature. The PdNTs annealed at higher temperatures exhibited negative shifts in their peak current potential for formic acid oxidation and increased activity at 0.3 V, which may be a result of grain growth and an associated increase in the expression of more active, low energy crystal planes as their surfaces become more coordinated.[8,68–70] Observations in the cyclic voltammograms in acid found in Figure 6A suggest that general particle-size-dependent crystallographic changes are present in the PdNTs after thermal treatments at elevated temperatures. Particle size effects have previously been reported for Pd for formic acid oxidation, with nanoparticles of intermediate size (5–9 nm) considered most active.[71,72] The two most active Bi-free PdNTs tested in this work were those annealed at 400 (5.8 nm) and 500 °C (11.6 nm), and their calculated grain sizes correspond loosely to the range of particle sizes reported to be the most active for carbon-supported Pd nanoparticles.[71,72]

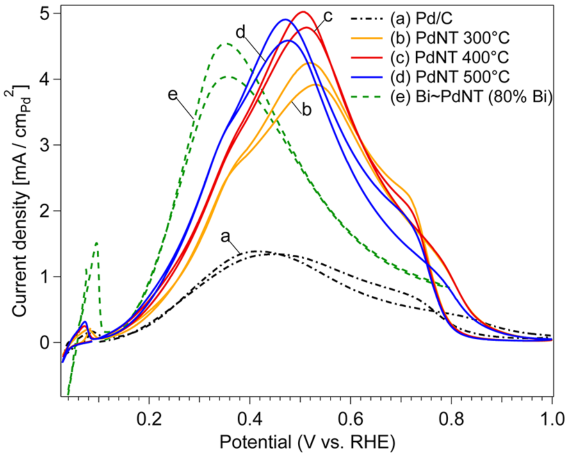

Figure 9. Area-normalized cyclic voltammograms recorded at 20 mV/s in 0.5 M H_2SO_4 and 0.5 M HCOOH for (a) commercial, carbon-supported Pd (20 wt % Pd), PdNTs annealed at (b) 300, (c) 400, (d) 500, and (e) Bi-decorated PdNTs annealed at 500 °C. Voltammograms are normalized to the available Pd area. Labels point to the anodic scans of the voltammograms.

The long-term stability of a catalyst is critical for its application within a direct formic acid fuel cell. Chronoamperometry is used to assess the stability of unmodified PdNTs annealed at 500 °C, Bi-modified PdNTs (80% Bi), and the commercial Pd/C by a 24 h potential hold at 0.2 V vs RHE, shown in Figure 10. Although the PdNTs annealed at 500 °C (Figure 10b) were highly active for formic acid oxidation, these extended surface catalysts destabilized rapidly over the course of the chronoamperometry experiment and were completely deactivated after 3 h; however, the modification of their surfaces with Bi adatoms (Figure 10a) drastically improved catalyst stability without significant penalty in mass activity. After 1 h of the potential hold at 0.2 V, the Bi-modified PdNTs (93.4 A/g_{Pd}) maintained a higher mass activity than Bi-free PdNTs (77.0 A/g_{Pd}) and the commercial Pd/C (79.7 A/g_{Pd}). After 3 h, the Bi-modified PdNTs (80% Bi) maintain 5 times the area-normalized current density as Pd/C (Figure 10c), whereas in the same time frame, the unmodified PdNTs completely deactivated. The Bi-modified PdNTs continued to outperform Pd/C by a factor of 2 after 24 h,

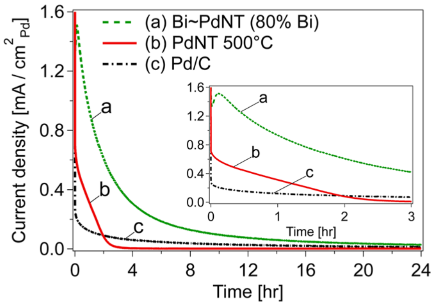

Figure 10. Chronoamperometric hold at 0.2 V vs RHE in 0.1 M $HClO_4$ and 1.0 M HCOOH without rotation. The current is normalized by the sample ECSA, which refers to available Pd.

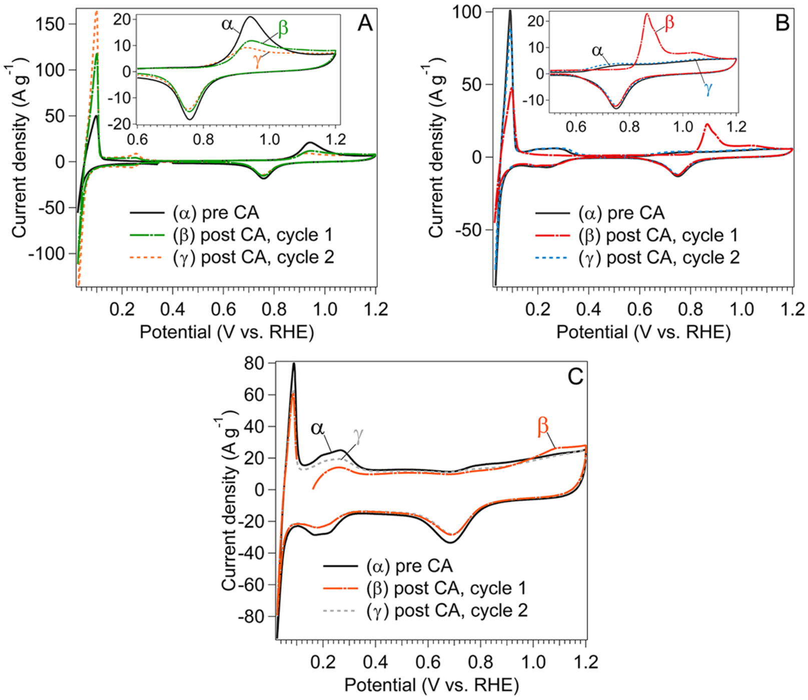

Figure 11. Cyclic voltammograms recorded in 0.1 M $HClO_4$ electrolyte at 20 mV/s for (A) Bi-modified PdNTs (80% Bi), (B) 500 °C PdNT, and (C) Pd/C immediately before and after a 24 h chronoamperometric hold at 0.2 V in 0.1 M $HClO_4$ and 1.0 M HCOOH.

although we observe a considerable reduction in the activity of all of the catalysts in this time frame.

A comparison of the cyclic voltammograms recorded immediately before and after the chronoamperometry (CA) experiment offers insight into the various destabilization modes operative for the different catalysts. In Figure 11A, it is apparent from the reduction in the area of the Bi oxide peak in the first voltammogram following the chronoamperometry experiment (Figure 11A,β) that Bi has desorbed from the catalyst surface during the stability experiment, similarly to that observed previously for Bi-modified Pd/C.[20] The emergence of the H-desorption features between 0.2 and 0.4 V in the first cycle following the CA experiment (Figure 11A,β) also indicate that more Pd sites are exposed because the initial Bi coverage decreased from 80% to ∼23%. This results in a suboptimal Bi coverage that we have shown to be less effective at promoting formic acid oxidation on these PdNTs than higher Bi adatom coverages. This is evident in Figure 8 because the formic acid oxidation activity decreases with reductions in surface Bi coverage below 80%.

The 500 °C PdNT in Figure 11B appears to have been inhibited by the formation of site-blocking adsorbates during the chronoamperometry experiment. The hydrogen desorption peaks initially observed on its clean surface prior to chronoamperometry are suppressed in the first voltammogram following chronoamperometry. The large oxidation feature at 0.87 V in this first cycle following chronoamperometry (Figure 11B,β) is thought to correspond to the removal of carbon monoxide.[73] There is also a noticeable oxidation feature at 1.05 V in the first scan following CA that is attributed to an interaction of palladium oxides and adsorbed intermediates.[74] Cycling this electrode once effectively cleaned its surfaces because its second cyclic voltammogram following chronoamperometry (Figure 11B,γ) was nearly indistinguishable from the voltammogram recorded prior to the stability experiment; the initial catalyst surface was restored after oxidizing the accumulated adsorbed species.

The Pd/C also lost activity during the CA experiment as a result of surface coverage by adsorbates as well as by a physical degradation that was not observed for the nanotube samples. In the first cycle after chronoamperometry (Figure 11C,β), the Pd/C has a small oxidation feature at 1.05 V described above for the unmodified PdNTs. In addition, there were considerable decreases in the charges of the Pd oxide reduction peak and the hydrogen desorption features that were not restored with cycling. This indicates a reduction in catalyst surface area and is likely the consequence of Pd dissolution into the acidic electrolyte.[10,75] Unlike the two PdNT samples, those with and without Bi modification, cycling the Pd/C electrode was not observed to restore the initial surface of the catalyst.

4. CONCLUSION

Palladium nanotubes were synthesized within alumina templates by a novel chemical vapor deposition technique from palladium acetylacetonate precursors at relatively low temperatures. The metal nanotubes were thermally annealed in a range of temperatures up to 500 °C in 4% H_2. The thermal treatment promoted a series of changes to the morphologies and surfaces of the nanotubes. The Pd nanotubes, agglomerates of fine Pd nanoparticles after synthesis, underwent grain growth with increases in heat treatment temperature and ultimately displayed improved specific activity for the oxidation of formic acid. The palladium nanotubes annealed at 500 °C (2.19 mA/cm^2) are 2.4 times more active than commercially available, carbon-supported Pd (0.91 mA/cm^2) at 0.3 V vs RHE.

The adsorption of Bi to the Pd nanotubes significantly improved their formic acid oxidation activity and stability. A maximum in specific activity of Bi-decorated Pd nanotubes was observed at 80% Bi coverage, and these optimum Bi-modified PdNTs (3.75 mA/cm^2) were over 4 times as active as Pd/C and nearly twice as active as the unmodified PdNTs at 0.3 V vs RHE. The addition of Bi adatoms was observed to drastically reduce the accumulation of site-blocking intermediates on the surface of the Pd nanotubes during chronoamperometry experiments, improving catalyst stability remarkably. The Bi-modified PdNTs were 5 times as active as Pd/C after 3 h of a chronoamperometric hold at 0.2 V vs RHE. In the same amount of time, Bi-free PdNTs deactivated completely, which was the result of surface coverage by reaction intermediates. These results strongly imply that the adsorption of Bi to the Pd nanotubes promotes the direct oxidation of formic acid by promoting a preferred molecule-binding geometry.

■ ASSOCIATED CONTENT

Ⓢ Supporting Information

The Supporting Information is available free of charge on the ACS Publications website at DOI: 10.1021/acscatal.5b01239.

> Scatter plot of palladium nanotube formic acid oxidation mass activity as a function of Bi adatom coverage (PDF)

■ AUTHOR INFORMATION

Corresponding Author

*E-mail: apapandr@utk.edu.

Notes

The authors declare no competing financial interest.

■ ACKNOWLEDGMENTS

Support of this work was provided by the NSF-funded TN-SCORE program, NSF EPS-1004083, under Thrust 2. STEM was conducted as part of a user proposal at ORNL's Center for Nanophase Materials Sciences (CNMS), which is an Office of Science User Facility. This research used resources of the Advanced Photon Source, a U.S. Department of Energy (DOE) Office of Science User Facility operated for the DOE Office of Science by Argonne National Laboratory under Contract No. DE-AC02-06CH11357.

■ REFERENCES

(1) Rice, C.; Ha, S.; Masel, R. I.; Waszczuk, P.; Wieckowski, A.; Barnard, T. *J. Power Sources* **2002**, *111*, 83−89.
(2) Rice, C.; Ha, S.; Masel, R. I.; Wieckowski, A. *J. Power Sources* **2003**, *115*, 229−235.
(3) Capon, A.; Parsons, R. *J. Electroanal. Chem. Interfacial Electrochem.* **1973**, *45*, 205−231.
(4) Peng, B.; Wang, H.-F.; Liu, Z.-P.; Cai, W.-B. *J. Phys. Chem. C* **2010**, *114*, 3102−3107.
(5) Bauskar, A. S.; Rice, C. A. *Electrochim. Acta* **2013**, *93*, 152−157.
(6) Adams, B. D.; Asmussen, R. M.; Ostrom, C. K.; Chen, A. *J. Phys. Chem. C* **2014**, *118*, 29903−29910.
(7) Llorca, M. J.; Feliu, J. M.; Aldaz, A.; Clavilier, J. *J. Electroanal. Chem.* **1994**, *376*, 151−160.
(8) Baldauf, M.; Kolb, D. M. *J. Phys. Chem.* **1996**, *100*, 11375−11381.
(9) Babu, P. K.; Kim, H. S.; Chung, J. H.; Oldfield, E.; Wieckowski, A. *J. Phys. Chem. B* **2004**, *108*, 20228−20232.
(10) Pan, Y.; Zhang, R.; Blair, S. L. *Electrochem. Solid-State Lett.* **2009**, *12*, B23−B26.
(11) Perales-Rondón, J. V.; Herrero, E.; Feliu, J. M. *J. Electroanal. Chem.* **2015**, *742*, 90−96.
(12) Wang, X.; Tang, Y.; Gao, Y.; Lu, T. *J. Power Sources* **2008**, *175*, 784−788.
(13) Morales-Acosta, D.; Ledesma-Garcia, J.; Godinez, L. A.; Rodríguez, H. G.; Álvarez-Contreras, L.; Arriaga, L. G. *J. Power Sources* **2010**, *195*, 461−465.
(14) Mazumder, V.; Chi, M.; Mankin, M. N.; Liu, Y.; Metin, O.; Sun, D.; More, K. L.; Sun, S. *Nano Lett.* **2012**, *12*, 1102−1106.
(15) Ho, S. F.; Mendoza-Garcia, A.; Guo, S.; He, K.; Su, D.; Liu, S.; Metin, O.; Sun, S. *Nanoscale* **2014**, *6*, 6970−6973.
(16) Ren, M.; Zhou, Y.; Tao, F.; Zou, Z.; Akins, D. L.; Yang, H. *J. Phys. Chem. C* **2014**, *118*, 12669−12675.
(17) Matin, M. A.; Jang, J.-H.; Kwon, Y.-U. *J. Power Sources* **2014**, *262*, 356−363.
(18) Sun, D.; Si, L.; Fu, G.; Liu, C.; Sun, D.; Chen, Y.; Tang, Y.; Lu, T. *J. Power Sources* **2015**, *280*, 141−146.
(19) Leiva, E.; Iwasita, T.; Herrero, E.; Feliu, J. M. *Langmuir* **1997**, *13*, 6287−6293.
(20) Bauskar, A. S.; Rice, C. A. *Electrochim. Acta* **2013**, *107*, 562−568.
(21) Perales-Rondón, J. V.; Ferre-Vilaplana, A.; Feliu, J. M.; Herrero, E. *J. Am. Chem. Soc.* **2014**, *136*, 13110−13113.
(22) Ferre-Vilaplana, A.; Perales-Rondón, J. V.; Feliu, J. M.; Herrero, E. *ACS Catal.* **2015**, *5*, 645−654.
(23) Busó-Rogero, C.; Perales-Rondón, J. V.; Farias, M. J. S.; Vidal-Iglesias, F. J.; Solla-Gullon, J.; Herrero, E.; Feliu, J. M. *Phys. Chem. Chem. Phys.* **2014**, *16*, 13616−13624.
(24) Cuesta, A. *ChemPhysChem* **2011**, *12*, 2375−2385.
(25) Cuesta, A.; Escudero, M.; Lanova, B.; Baltruschat, H. *Langmuir* **2009**, *25*, 6500−6507.
(26) Neurock, M.; Janik, M.; Wieckowski, A. *Faraday Discuss.* **2009**, *140*, 363−378.
(27) Neurock, M.; Janik, M.; Wieckowski, A. *Faraday Discuss.* **2009**, *140*, 363−378.
(28) Wang, H.-F.; Liu, Z.-P. *J. Phys. Chem. C* **2009**, *113*, 17502−17508.
(29) Herron, J. A.; Scaranto, J.; Ferrin, P.; Li, S.; Mavrikakis, M. *ACS Catal.* **2014**, *4*, 4434−4445.
(30) Steinmann, S. N.; Michel, C.; Schwiedernoch, R.; Filhol, J.-S.; Sautet, P. *ChemPhysChem* **2015**, DOI: 10.1002/cphc.201500187.
(31) St. John, S.; Angelopoulos, A. P. *Electrochim. Acta* **2013**, *112*, 258−268.
(32) Chen, Z.; Waje, M.; Li, W.; Yan, Y. *Angew. Chem., Int. Ed.* **2007**, *46*, 4060−4063.
(33) Van der Vliet, D. F.; Wang, C.; Tripkovic, D.; Strmcnik, D.; Zhang, X. F.; Debe, M. K.; Atanasoski, R. T.; Markovic, N. M.; Stamenkovic, V. R. *Nat. Mater.* **2012**, *11*, 1051−1058.
(34) Komanicky, V.; Chang, K. C.; Menzel, A.; Markovic, N. M.; You, H.; Wang, X.; Myers, D. *J. Electrochem. Soc.* **2006**, *153*, B446−B451.
(35) Shao, Y.; Yin, G.; Gao, Y. *J. Power Sources* **2007**, *171*, 558−566.
(36) Darling, R. M.; Meyers, J. P. *J. Electrochem. Soc.* **2003**, *150*, A1523−A1527.
(37) Wang, S.; Jiang, S. P.; Wang, X.; Guo, J. *Electrochim. Acta* **2011**, *56*, 1563−1569.
(38) Sun, S.; Jaouen, F.; Dodelet, J.-P. *Adv. Mater.* **2008**, *20*, 3900−3904.
(39) Zhou, W.-P.; Li, M.; Koenigsmann, C.; Ma, C.; Wong, S. S.; Adzic, R. R. *Electrochim. Acta* **2011**, *56*, 9824−9830.
(40) Papandrew, A. B.; Atkinson, R. W., III; Goenaga, G. A.; Kocha, S. S.; Zack, J. W.; Pivovar, B. S.; Zawodzinski, T. A., Jr. *J. Electrochem. Soc.* **2013**, *160*, F848−F852.
(41) Wang, R.; Higgins, D. C.; Prabhudev, S.; Lee, D. U.; Choi, J.-Y.; Hoque, M. A.; Botton, G. A.; Chen, Z. *J. Mater. Chem. A* **2015**, *3*, 12663−12671.
(42) Atkinson, R. W., III; Unocic, R. R.; Unocic, K. A.; Veith, G. M.; Zawodzinski, T. A., Jr.; Papandrew, A. B. *ACS Appl. Mater. Interfaces* **2015**, *7*, 10115−10124.
(43) Cherstiouk, O. V.; Simonov, P. A.; Savinova, E. R. *Electrochim. Acta* **2003**, *48*, 3851−3860.
(44) Ravel, B. *EXAFS Analysis with FEFF and FEFFIT*; University of Washington: Pullman, WA, 2001; Vol. 2.
(45) Garsany, Y.; Baturina, O. A.; Swider-Lyons, K. E.; Kocha, S. S. *Anal. Chem.* **2010**, *82*, 6321−6328.
(46) Alia, S. M.; Jensen, K. O.; Pivovar, B. S.; Yan, Y. *ACS Catal.* **2012**, *2*, 858−863.
(47) Vidaković, T.; Christov, M.; Sundmacher, K. *Electrochim. Acta* **2007**, *52*, 5606−5613.
(48) Clavilier, J.; Feliu, J. M.; Aldaz, A. *J. Electroanal. Chem. Interfacial Electrochem.* **1988**, *243*, 419−433.

(49) Rodríguez, P.; Solla-Gullón, J.; Vidal-Iglesias, F. J.; Herrero, E.; Aldaz, A.; Feliu, J. M. *Anal. Chem.* **2005**, *77*, 5317−5323.
(50) Rodríguez, P.; Herrero, E.; Solla-Gullón, J.; Vidal-Iglesias, F. J.; Aldaz, A.; Feliu, J. M. *Electrochim. Acta* **2005**, *50*, 4308−4317.
(51) Solla-Gullón, J.; Rodríguez, P.; Herrero, E.; Aldaz, A.; Feliu, J. M. *Phys. Chem. Chem. Phys.* **2008**, *10*, 1359−1373.
(52) Ziemecki, S. B.; Jones, G. A.; Swartzfager, D. G.; Harlow, R. L.; Faber, J., Jr. *J. Am. Chem. Soc.* **1985**, *107*, 4547−4548.
(53) McCaulley, J. A. *Phys. Rev. B: Condens. Matter Mater. Phys.* **1993**, *47*, 4873−4879.
(54) McCaulley, J. A. *J. Phys. Chem.* **1993**, *97*, 10372−10379.
(55) Papandrew, A. B.; Chisholm, C. R. I.; Zecevic, S. K.; Veith, G. M.; Zawodzinski, T. A. *J. Electrochem. Soc.* **2012**, *160*, F175−F182.
(56) Papandrew, A. B.; Wilson, D. L., III; Cantillo, N. M.; Hawks, S.; Atkinson, R. W., III; Goenaga, G. A.; Zawodzinski, T. A., Jr. *J. Electrochem. Soc.* **2014**, *161*, F679−F685.
(57) Harada, M.; Asakura, K.; Ueki, Y.; Toshima, N. *J. Phys. Chem.* **1992**, *96*, 9730−9738.
(58) Arenz, M.; Mayrhofer, K. J. J.; Stamenkovic, V.; Blizanac, B. B.; Tomoyuki, T.; Ross, P. N.; Markovic, N. M. *J. Am. Chem. Soc.* **2005**, *127*, 6819−6829.
(59) Mayrhofer, K. J. J.; Blizanac, B. B.; Arenz, M.; Stamenkovic, V. R.; Ross, P. N.; Markovic, N. M. *J. Phys. Chem. B* **2005**, *109*, 14433−14440.
(60) Takasu, Y.; Iwazaki, T.; Sugimoto, W.; Murakami, Y. *Electrochem. Commun.* **2000**, *2*, 671−674.
(61) Urchaga, P.; Baranton, S.; Coutanceau, C.; Jerkiewicz, G. *Langmuir* **2012**, *28*, 3658−3663.
(62) Tateishi, N.; Yahikozawa, K.; Nishimura, K.; Suzuki, M.; Iwanaga, Y.; Watanabe, M.; Enami, E.; Matsuda, Y.; Takasu, Y. *Electrochim. Acta* **1991**, *36*, 1235−1240.
(63) Nag, N. K. *J. Phys. Chem. B* **2001**, *105*, 5945−5949.
(64) Jerkiewicz, G.; Zolfaghari, A. *J. Electrochem. Soc.* **1996**, *143*, 1240−1248.
(65) Grdeń, M.; Łukaszewski, M.; Jerkiewicz, G.; Czerwiński, A. *Electrochim. Acta* **2008**, *53*, 7583−7598.
(66) Kim, B.-J.; Kwon, K.; Rhee, C. K.; Han, J.; Lim, T.-H. *Electrochim. Acta* **2008**, *53*, 7744−7750.
(67) Parsons, R.; VanderNoot, T. *J. Electroanal. Chem. Interfacial Electrochem.* **1988**, *257*, 9−45.
(68) Vidal-Iglesias, F. J.; Arán-Ais, R. M.; Solla-Gullón, J.; Garnier, E.; Herrero, E.; Aldaz, A.; Feliu, J. M. *Phys. Chem. Chem. Phys.* **2012**, *14*, 10258−10265.
(69) Figueiredo, M. C.; Solla-Gullón, J.; Vidal-Iglesias, F. J.; Nisula, M.; Feliu, J. M.; Kallio, T. *Electrochem. Commun.* **2015**, *55*, 47−50.
(70) Bertin, E.; Garbarino, S.; Guay, D.; Solla-Gullón, J.; Vidal-Iglesias, F. J.; Feliu, J. M. *J. Power Sources* **2013**, *225*, 323−329.
(71) Zhou, W. P.; Lewera, A.; Larsen, R.; Masel, R. I.; Bagus, P. S.; Wieckowski, A. *J. Phys. Chem. B* **2006**, *110*, 13393−13398.
(72) Zhou, W.; Lee, J. Y. *J. Phys. Chem. C* **2008**, *112*, 3789−3793.
(73) Miyake, H.; Hosono, E.; Osawa, M.; Okada, T. *Chem. Phys. Lett.* **2006**, *428*, 451−456.
(74) Hoshi, N.; Kida, K.; Nakamura, M.; Nakada, M.; Osada, K. *J. Phys. Chem. B* **2006**, *110*, 12480−12484.
(75) Capon, A.; Parsons, R. *J. Electroanal. Chem. Interfacial Electrochem.* **1973**, *44*, 239−254.